Estimating Evapotranspiration From Satellite Using Easily Obtainable Variables: A case study over the Southern Great Plains, U.S.A.

Ali L. Yagci, and Joseph A. Santanello

***Abstract*—Evapotranspiration (ET) is a critical component of the Earth's water budget, a critical modulator of land-atmosphere (L-A) interactions, and also plays a crucial role in managing the Earth's energy balance. In this study, the feasibility of generating spatially-continuous daily evaporative fraction (EF) and ET from minimal remotely-sensed and meteorological inputs in a trapezoidal framework is demonstrated. A total of four variables, Normalized Difference Vegetation Index (NDVI), Land surface temperature (T_s), gridded daily average temperature (T_a) and elevation (z) are required to estimate EF. Then, ET can be estimated with the available soil heat flux (G) and net radiation (Rn) data. Firstly, the crucial model variable, $T_s - T_a$, is examined how well it characterizes the variation in EF using in situ data recorded at two eddy correlation flux towers in Southern Great Plains, U.S.A in 2011. Next, accuracy of satellite-based T_s are compared to ground-based T_s. Finally, EF and ET estimates are validated. The results reveal that the model performed satisfactorily in modeling EF and ET variation at winter wheat and deciduous forest during the high evaporative months. Even though the model works best with the observed MODIS-T_s as opposed to temporally interpolated T_s, results obtained from interpolated T_s are able to close the gaps with reasonable accuracy. Due to the fact that $T_s - T_a$, is not a good indicator of EF outside the growing season when deciduous forest is dormant, potential improvements to the model are proposed to improve accuracy in EF and ET estimates at the expense of adding more variables.**

***Index Terms*— Deciduous Forest, Evaporative Fraction, Evapotranspiration, Land Surface Temperature, NDVI, Trapezoid Method, Wheat.**

I. Introduction

EVAPOTRANSPIRATION (ET) represents the terrestrial water released back to atmosphere through soil evaporation and plant transpiration in the form of water vapor (mm units), which is also referred to as Latent Heat Flux (LE) in energy units (W/m-2). It is one of the key components of the Earth's water budget after precipitation (P), a critical modulator of land-atmosphere (L-A) interactions, and also plays also a crucial role in managing the Earth's energy balance.

There is a strong demand for improved daily ET products on the order of 1 km spatial resolution (i.e., the upper end of typical land surface model resolution) for hydrological applications, climate studies [1] and diagnosis of L-A interactions [2]. As a result, a considerable number of ET products have been developed over recent years, and a suite of global ET products has also been recently been intercompared in the framework of LandFlux-EVAL initiative [3], [4] and the Global Energy and Water Cycle Exchanges (GEWEX) LandFlux project [5]. These studies have concluded that large uncertainties exist in the current global ET estimates due to accuracy of input forcing data and parameterizations, and further development of higher accuracy ET products is essential and an immediate concern [1], [6]. Furthermore, Xia et al. [7] concluded that land surface models (LSMs) run in the North American Land Data Assimilation System project phase 2 (NLDAS-2) cannot simulate ET well on a daily step for deciduous and evergreen forests and croplands.

Broadly, current ET estimation methods can be separated into three distinct groups: (1) diagnostic, (2) LSMs and (3) reanalyses [1]. The diagnostic approaches are rather empirical models that utilize satellite-measured land surface temperatures and vegetation indices in the derivation of fluxes. They are relatively simple models dedicated solely to flux estimation [3]. Conversely, LSMs are more sophisticated physics packages that attempt to fully solve surface energy and water balance terms. When LSMs are coupled with an atmospheric model and assimilate (primarily atmospheric) observations, it is often called "reanalysis" [3]. The advantage of diagnostic ET models over LSMs is that the latter demands heavy load of surface and subsurface observations, model calibration and parameterizations, while the former requires comparatively less a priori knowledge of the surface and subsurface conditions [8]. The advantage of diagnostic approaches over reanalyses lie primarily in increased spatial resolution in diagnostic methods that utilize the native resolution of satellite-based inputs (e.g. 1km-scale) versus that of a large atmospheric grid cell (~50km).

Land surface temperature (T_s) derived from the thermal infrared (TIR) region (3-14 μm) is a critical diagnostic variable that contains information on the surface energy balance, terrestrial water stress and subsequently ET. Soil temperature (and thus T_s) increases with decreasing soil moisture, whereas a lack of water content in plant's root zone leads to stomatal closure to minimize water loss through transpiration, and eventually elevated canopy temperatures [9]. As a result, T_s is a good indicator of the surface moisture condition, energy

This paragraph of the first footnote will contain the date on which you submitted your paper for review. "This work was supported by the NASA Postdoctoral Program under Grant, NNH15C048B".

The authors are with Hydrological Sciences Laboratory (617), Goddard Space Flight Center, National Aeronautics and Space Administration, Greenbelt, Maryland, 20771, U.S.A. (e-mail: yagciali2002@gmail.com; ali.l.yagci@nasa.gov; joseph.a.santanello@nasa.gov).

balance, and ET.

Among the diagnostic models that utilize T_s and vegetation index, there are two ways to determine ET based on the satellite remote sensing data. The first way is to compute evaporative fraction (EF) and then multiply EF with the total available energy. Triangle [10] and trapezoidal [11] methods can be given as an example of the this category. The second way is to calculate sensible heat flux (H) in the first step, and then derive Latent Heat (LE) as a residual of the energy balance equation ($LE = R_n - G - H$) as in the Two-Source Energy Balance model (TSEB) [12], TSEB's extension, the Atmosphere-Land Exchange Inverse (ALEXI) [8], the Surface Energy Balance Algorithm for Land (SEBAL) [13] and a variant of SEBAL, Mapping EvapoTRanspiration with Internalized Calibration (METRIC) [14]. Further, TSEB and ALEXI partition ET into evaporation and transpiration components using fractional vegetation cover (*fr*) while other diagnostic models provide only a composite ET estimate. A recent intercomparison among these diagnostic models reported that triangle method was the worst performing model, and errors were quite large in comparison to TSEB and METRIC [15].

In summary, the accuracy and resolution of the current ET products is not adequate to satisfy the needs of hydrological, land surface and climate modelers. Moreover, the need for a large amount of forcing data and in-situ measurements, usually available only locally or in coarse resolution, to run the ET models contributes to uncertainties and errors in the final ET products [5], [16]. The objective of this study is to therefore demonstrate the feasibility of generating daily, high resolution (e.g., 1km), spatially continuous regional EF and ET estimates using only minimal satellite inputs.

II. DATA AND METHODS

A. Trapezoidal Model

Moran et al. [11] demonstrated that measurements of *fr* and land surface minus air temperature ($T_s - T_a$) would theoretically form a trapezoidal shape when plotted together in a two dimensional space (Fig. 1) and termed the concept, vegetation index-temperature trapezoid (VITT). Going left to right within this shape, soil moisture conditions change from wet to dry. The edges of this shape represent hydrological extremes (wet and dry conditions).

The VITT concept postulates that P1 and P3 are the vertices of the trapezoid that represent well-watered vegetation and bare soil, respectively, while P2 and P4 indicate water-stressed vegetation and bare soil. Linear lines connecting P2 to P4, and P1 to P3 form dry and wet edges, respectively, and these edges can be used to constrain EF estimates such that EF is set to 0 and 1 along the dry and wet edge.

Applications of this method have been limited, as it requires extensive accurately-measured in-situ observations and assumptions to estimate trapezoid vertices by the deterministic equations [11]. However, these equations can be circumvented and the wet and dry edges can be extracted from satellite-based NDVI and T_s products and daily average air temperature (T_a), as demonstrated in mangrove forests of Everglades National Park, Florida, U.S.A. [17], [18]. NDVI can be used to replace *fr*, given their close relationship [19], [20]. Priestley-Taylor coefficient (α) can be estimated from dry and wet edges where α is 0 and 1.26 [21], respectively, using the (1), (2), and (3) below.

$$(T_s - T_a)_{wet} = \frac{(NDVI_m - b_{wet})}{a_{wet}} \quad (1)$$

$$(T_s - T_a)_{dry} = \frac{(NDVI_m - b_{dry})}{a_{dry}} \quad (2)$$

where a and b are slope and intercept of the lines on the wet and dry edges. Dry and wet subscripts in 1, 2 and 3 show that equation terms belong to dry and wet edges, respectively. $(T_s - T_a)_{dry}$ and $(T_s - T_a)_{wet}$ is the calculated value of $T_s - T_a$ on the dry and wet edge, respectively.

Later, α can be interpolated using the following equation:

$$\alpha_m = \frac{(T_s - T_a)_{dry} - (T_s - T_a)_m}{(T_s - T_a)_{dry} - (T_s - T_a)_{wet}} \quad (3)$$

where $(T_s - T_a)_m$ is the observed value of $T_s - T_a$ for the pixel of interest. (3) will be run for all the pixels within the entire remote sensing scene. Later, EF can be calculated with the Priestley-Taylor equation as follows:

$$EF_m = \alpha_m \cdot \frac{\Delta}{\Delta + \gamma} \quad (4)$$

where Δ (kPa °C^{-1}) and γ (kPa °C^{-1}) are the slope of saturation vapor pressure curve at the air temperature (T_a in °C) and psychometric constant which can be computed by (5) and (6), respectively [22].

$$\Delta = \frac{4098 \cdot \left[0.6108 \cdot \exp\left(\frac{17.27 \cdot T_a}{T_a + 237.3}\right)\right]}{(T_a + 237.3)^2} \quad (5)$$

$$\gamma = 0.665 \times 10^{-3} \cdot P \quad (6)$$

For γ calculation, atmospheric pressure (P) is required and varies as a function of elevation above sea level (z) and daily average air temperature (T_a) as shown in (7) [22]. Z is derived from the 1-km digital elevation data which is resampled from the 90m Shuttle Radar Topography Mission data [23].

$$P = 101.3 \cdot \left[\frac{(T_a + 273.16) - 0.0065 \cdot z}{(T_a + 273.16)}\right]^{5.26} \quad (7)$$

Finally, ET can be estimated from the following equation;

$$ET_m = EF_m \cdot (R_n - G) \quad (8)$$

where R_n is surface net available energy and G is soil heat flux.

Using NDVI and T_s products from the Moderate Resolution Imaging Spectroradiometer (MODIS) instrument onboard NASA's Terra and Aqua satellites and the methodology outlined here, it is possible to construct a trapezoid shape and

approximate wet and dry edges on a daily basis in a fully automated fashion. The scatterplots of the entire MODIS tile (i.e., h10v05) encompassing the Southern Great Plains is shown in Fig. 2 along with critical points of the trapezoid and the linear lines of dry and wet edge. The trapezoid shapes in A and B of Fig. 2 are derived from the MODIS-T_s product acquired on July 28, 2011 from Terra and Aqua, respectively. To compute the vertices of the trapezoid, the pixels along the bare soil and full-canopy vegetation NDVIs are extracted and independently classified as bare soil and full-cover vegetation pixels (Fig. 3). In the model, bare soil and full-canopy vegetation NDVIs are set to 0.2 [24] and 99th percentile of the scene (e.g., 0.877 on as in Figs. 3 & 4), respectively. Next, based on $T_s - T_a$ values, selected points (Fig. 3) are grouped into separate classes with an interval size of 0.5 °C and number of points in each class is recorded. In the next step, classes less than 10 points are discarded. Among the remaining classes, those with the minimum and maximum $T_s - T_a$ values are selected to represent wet and dry points. For each scene, this process is run twice separately for bare soil and full-canopy vegetation pixels. After, $T_s - T_a$ values of P1, P2, P3 and P4 end points are found (Figs. 2 & 3), the slope and intercept of linear lines characterizing wet and dry edges can be computed. Following (1) to (8), EF and ET maps can then be constructed. All the listed operations above are fully automated in that no user interaction is required during the model run. The model is run twice daily; one for MODIS-Terra and the other for MODIS-Aqua products.

Scatterplots shown in Figs. 2 and 3 are automatically outputted from the model in order to see how well the vertices of trapezoid are constructed with respect to the shape of the point cloud because it is most likely that outlier points such as very low $T_s - T_a$ values (Fig. 2) can be mistakenly selected to form critical points (i.e., P1, P2, P3 and P4). These low $T_s - T_a$ values are due to undetected sub-pixel or full-pixel clouds and cloud shadows in the thermal imagery. In summary, there is no need for in situ measurements of variables that drive four equations [11] to compute the four vertices of the trapezoid. For this reason, the trapezoid model can be fully automated to produce spatially-distributed EF and ET maps with minimal satellite inputs.

B. Validation Sites and Data

Two ground sites, EF-14 and EF-21, in the U.S. Southern Great Plains (SGP) were selected to validate model estimates. These sites were established by the Department of Energy's (DOE) under the Atmospheric Radiation Measurement (ARM) program. The crop type at EF-14 site is winter wheat (Fig. 4-A), while forest (e.g., mixed deciduous forest) dominates the EF-21 site (Fig. 4-B). According to Köppen-Geiger classification, both validation sites are characterized by Temperate Humid climate with hot summers (Cfa).

Half-hourly flux observations of surface energy balance terms (i.e.; LE, H, R_n and G) measured in 2011 were retrieved from the ARM's archive website (http://www.archive.arm.gov/discovery/). LE and H flux observations are measured by the Eddy correlation (ECOR) method at 3 m (EF-14) and 15 m (i.e., 3 m above canopy, EF-21) height above ground [25], [26], while measurement of G, R_n as well as all surface radiation budget terms [27], [28] were collected by the surface energy balance system (SEBS) co-installed with ECOR system at the both flux towers. SEBS systems were installed on October 1, 2010 and collocated with each ECOR system at the ARM-SGP sites. ECOR and SEBS measurements undergo quality assurance steps and every half-hourly observation has a quality-control flag attached. Quality flag value of zero, "0", indicates that flux measurement passes all quality tests and is of high quality. Therefore, observations without a zero quality flag were discarded from the analysis.

EF, defined as ratio of LE to the available net energy at the surface, can be calculated by the following formula:

$$EF = \frac{\sum_0^n LE}{\sum_0^n (R_n - G)} \tag{9}$$

where R_n, G and LE is the sum of daytime net radiation, soil heat flux and latent heat measurements, respectively. Daytime is defined as the time period when 30 minute-averaged incoming shortwave radiation observations ($S\downarrow$) have a positive value in W/m^{-2} units. Due to the gaps in the flux tower data, diurnal EFs computed from less than fifteen, "15", half-hourly observations were removed from the validation.

All terms in energy balance equation are individually measured by ECOR and SEBS systems, but full-closure in energy balance are not usually achieved due to various reasons such as ECOR measurements under low wind speeds (less 1.5 m/s) and non-steady atmospheric conditions, omission of canopy energy storage in energy balance and sonic anemometer frequency measurement limitations [29]. Limitations in ECOR instrument are respectively causes 5% and 6% uncertainty in H and LE [29], and energy balance closure rate ($[H + LE]/[R_n - G]$) typically varies between 0.75 and 0.9 [29], [30]. Therefore, only diurnal EFs were kept for model validation when daytime energy balance closure rate is between 0.5 and 1. Of the remaining diurnal EFs, average daytime energy balance closure at both sites was 0.81 (81%) in 2011. Furthermore, both clear-sky and cloudy were retained in the study in order to test how well the model predicts the diurnal EF and ET under both clear-sky and cloudy conditions.

Stefan-Boltzmann law relates the total energy flux emitted from a surface to the surface skin temperature, and after rearranging the terms in the Stefan-Boltzmann formula, T_s can be calculated as follows:

$$T_s = \left[\frac{L\uparrow}{\varepsilon \cdot \sigma}\right]^{1/4} \tag{10}$$

where σ is the Stefan–Boltzmann constant (5.670x 10^{-8} W m^{-2} K^{-4}), ε is the surface emissivity and $L\uparrow$ is the surface outgoing longwave radiation. ε of flux towers were extracted from 100-m the Advanced Spaceborne Thermal Emission and Reflection Radiometer (ASTER) Global Emissivity Dataset [31].

In addition to observations of surface energy balance terms, 30-minute averaged air temperature (T_a) measurements [32],

[33] as required by the trapezoid method is collected at 2m height by the Surface Meteorological Instrumentation (MET) were also downloaded from the ARM's archive website.

C. MODIS NDVI Product

1-km 16-day NDVI composites (i.e., MOD13A2.005) of the MODIS tile number, h10v05, and the year, 2011, were retrieved from the Land Processes Distributed Active Archive Center (LPDAAC; https://lpdaac.usgs.gov/). The NDVI data were acquired by the MODIS instrument onboard Terra. Among the NDVI observations in a 16-day period, one clear-sky observation with the smallest view angle is selected to represent that 16-day period, and day of year (DOY) of that clear observation is recorded in the DOY layer [34].

NDVI products come with the detailed quality assessment (QA) layers, which hold critical quality information about each pixel of the scene. According to QA layers, pixels labeled with cloud, cloud shadows, cloud adjacent, snow/ice and heavy aerosols were masked out. Further, based on DOY of each NDVI observation, daily NDVI products were derived from the 16-day NDVI products by temporal interpolation. Due to small gaps (e.g., 0-10% of the MODIS scene, h10v05) emerged from the removal of NDVI pixels that don't fit the QA criteria above, two preceding and following 16-day periods were utilized to fill these gaps in the NDVI products.

D. MODIS T_s Products

Daily 1-km MODIS-T_s products acquired by both Terra (i.e., MOD11A1.005) and Aqua (i.e., MYD11A1.005) were downloaded from the LPDAAC website. Similar to the MODIS-NDVI products, MODIS-T_s products come with quality control (QC) layers [35]. Observations specified as "not produced due to clouds or other than clouds" and "emissivity and T_s errors exceeding 3K" in QC layers were removed. However, this QC masking process caused large gaps in the resulting T_s products. Thus, the remaining clear-sky observations are utilized to fill these gaps by temporal interpolation. Interpolation interval is set to 4 days given that T_s changes rapidly (unlike NDVI), and good correspondence (Figs. 8 & 9) and comparable errors (Table I) were found after interpolated T_s were compared to ground-based T_s. If there are not two clear-sky observations within the 9-day period, the T_s observation is not filled by interpolation.

E. Air Temperature (T_a)

Version 2 daily minimum and maximum air temperatures were retrieved from the Daily Surface Weather and Climatological Summaries (Daymet) dataset (https://daymet.ornl.gov/). Daymet consists of gridded near-surface (e.g., 2m) estimates of daily meteorological parameters including air temperature, precipitation, humidity, shortwave radiation and snow water equivalent at a 1-km resolution for North America [36]. Minimum and maximum air temperatures recorded daily at ground-based meteorological stations are spatially interpolated based on the spatial convolution of a truncated Gaussian weighting filter algorithm to produce daily 1-km spatially continuous fields of air temperature [37].

Daily average air temperature (T_a) used in the model is calculated by the following formula:

$$T_a = \frac{(T_{min} + T_{max})}{2} \quad (11)$$

where Tmin and Tmax daily minimum and maximum air temperature measured at 2-m height, respectively.

III. Results

The results are organized as follows: First, we report on the sensitivity of the diurnal $T_s - T_a$ relationship to α and EF variability throughout 2011. Then, we demonstrate how well satellite-derived instantaneous morning and afternoon T_s would represent diurnal mean T_s. Last, modeled EFs are compared to EFs observed at the flux towers.

A. Daily relationship of $T_s - T_a$ to α and EF

Because $T_s - T_a$ is the most crucial relationship in the trapezoidal model we begin by quantifying the sensitivity of various definitions of $T_s - T_a$ to α and EF in 2011 using in situ observations collected at both ground sites. The results demonstrate that the best EF was best predicted by diurnal-averaged $T_s - T_a$, then instantaneous $T_s - T_a$ collected at the Aqua satellite overpass (13:00 at EF-14 and 13:06 at EF-21) and performed the worst using instantaneous $T_s - T_a$ collected at the Terra satellite overpass (10:55 at EF-14 and 10:52 at EF-21). Because the best results were achieved with diurnal-averaged $T_s - T_a$ (Figs. 6 & 7), the results of instantaneous $T_s - T_a$ obtained at the Terra and Aqua overpasses are not shown here.

Time series of $T_s - T_a$ (Fig. 5) split into two parts depending on whether or not vegetation is active. For the deciduous forest site, EF-21, the largest rate of NDVI increase and decrease were approximated as the start of season (SOS) and end of season (EOS), respectively. Thus, SOS and EOS were set to the 96th day and 330th day of 2011, respectively (Fig. 5). Known wheat planting and harvesting dates in 2011 were selected to represent the SOS and EOS, also shown in Figure 5. Winter wheat planted in 318th day of 2010 was harvested by the 165th day of 2011 and re-planted by the 311th day of 2011. After the harvest until replanting of wheat in 2011, the field was a mix of bare soil and ungrazed grass.

NDVI profiles of the winter wheat and deciduous forest sites suggest that suddenly increase and end of gradual senescence identified as SOS and EOS, respectively, are clearly visible in NDVI time series of deciduous forest (Fig. 5). However, similar rate of increase and slow decrease appeared in NDVI time series of wheat pixel, but they don't match known wheat planting and harvesting dates because rainfall received shortly before and after the wheat harvesting date (Fig. 5) greened up the surrounding pasture, whose signal were also included in the large satellite view. The results suggest that coarse resolution NDVI time series cannot accurately capture sub-pixel winter wheat crop planting practices.

The results indicate that $T_s - T_a$ alone explained 79% and 80% variation in α and EF (Fig. 6-A & -C) during the 2011 growing season at EF-21, respectively. However, $T_s - T_a$ was

not a good indicator of both α and EF outside the growing season when deciduous forest was dormant (Fig 6-B & -C). Overall, $T_s - T_a$ was negatively correlated with both α and EF, meaning that high $T_s - T_a$ indicates low α and EF. In other words, both α and EF decrease by going from left to right within the trapezoid space as employed in the model. Except for the days following a major precipitation (PRCP) event (> 3 mm), EF hovered slightly around a constant value of 0.1, while α fluctuated around a constant value of 0.20. PRCP amounts accumulated in the last two days are shown with arrows in Figure 6-B & -D, and relatively high EFs following major PRCP events can also be seen in Fig. 5 for EF-21. On these days, both α and EF substantially differed from the rest of observations. When the weather was dry or PRCP amount is less than 3 mm outside the growing season, α and EF remained relatively flat while $T_s - T_a$ changed from 0 to 7.

In parallel to observed relationship at EF-21, $T_s - T_a$ was negatively, yet relatively weak, correlated with both α and EF at EF-14. Because most crop development stages (i.e., planting, emergence, fruiting and harvest) of winter wheat occurred when temperature was cold, $T_s - T_a$ accounted for 26% and 18% variances in α and EF, respectively. On the other hand, 51% and 50% variations in α and EF were explained by $T_s - T_a$ outside the growing season of winter wheat when evaporative demand was high.

B. Comparison of instantaneous MODIS-T_s with ground-based diurnal mean T_s

Because the relationship of diurnal-mean $T_s - T_a$ to α and EF was discussed in the previous section, a comparison was also made between instantaneous satellite-derived T_s and ground-based diurnal-average T_s to see how well one time remotely-sensed T_s measurement would represent the daytime T_s average. It can also serve to validate satellite-based T_s with ground-based T_s. In this case, it is expected to see a positive bias, that is; MODIS-T_s should be higher than ground-based T_s because a diurnal average consists of low T_s observations collected after sunrise and before sunset. Comparison is restricted to the days when ground-based EF and ET data are available.

The results demonstrate that MODIS-T_s accounts for 91%-94% in ground-based T_s at both sites (Figs. 8 & 9). Gap filling of satellite-based T_s by interpolation introduces larger errors (Table I) in MODIS-T_s at EF-14 than EF-21. Variance in ground-based T_s explained by MODIS-T_s reduced to 78%-80% at EF-14, whereas 88%-89% variance was accounted for at EF-21 (Figs. 8 & 9). However, this could be attributed to small number days considered in the comparison at EF-21.

Both morning and afternoon MODIS-T_s performed equally effective at characterizing ground-based T_s in 2011. As expected, both morning and afternoon MODIS-T_s exhibited a positive bias, and the bias in afternoon T_s was larger than morning T_s (Table I). On average, morning T_s (afternoon T_s) was as high as 1.84 °C (4.77 °C) and 1.36°C (3.04°C) than diurnal-mean T_s (Table I) at EF-14 and EF-21, respectively. Gap filling of T_s by interpolation additionally increased this positive bias by 2.5 °C and 0.1-0.5 °C at EF-14 and EF-21, respectively (Table I). Overall, the positive bias between MODIS-T_s and ground-T_s was smaller at EF-21 than EF-14 because MODIS sensor views an area of 1km^2, which is a mix of deciduous forest and open water at EF-21 (Fig. 4-B). Because the surface is usually colder over lakes (as evaporation is at the potential level), the presence of lakes within the MODIS pixel at EF-21 reduces the positive bias in comparison to EF-14 site.

For a more meaningful comparison, the biases were removed from the root mean square error (RMSE) (Table I) because MODIS T_s is instantaneous, and ground T_s is diurnally averaged. Results show that bias-corrected RMSEs of morning (afternoon) T_s were 2.93°C (2.49°C) and 2.49°C (2.60°C) at EF-14 and EF-21, respectively. RMSEs in afternoon T_s were relatively smaller compared to morning T_s at EF-14, and the opposite result was achieved at EF-21. Finally, interpolation of T_s from observed T_s within 4 preceding and following days caused larger errors at EF-14 than EF-21. Bias-removed RMSEs of morning and afternoon T_s were 4.75 °C and 4.51 °C at EF-14, respectively. In the same way, RMSEs in morning and afternoon T_s were 3.07 °C and 3.24 °C at EF-21, respectively. Overall, RMSEs in the interpolated T_s at EF-21 were considerably smaller than RMSEs at EF-14, and this could be attributed to farming practices at the cropland site.

It is worth pointing out that although satellite-derived T_s is directly compared with a flux tower T_s (Fig. 8 & 9), the footprint mismatch and inclusion of all-weather conditions (i.e., cloudy and clear-sky) in the diurnal mean can contribute to discrepancy between the two. For example, T_s acquired by MODIS are an aggregate value of a 1 km^2 heterogeneous area on the ground, and diurnal mean T_s consists of half-hourly T_s observations obtained under both clear-sky and cloudy conditions.

C. Model validation with ground truth

Modeled EF estimates were multiplied with available energy (Rn-G) recorded at two validation sites to estimate ET. Later, both modeled EF and ET were compared to observed EF and LE at EF-21 (Fig. 10) and EF-14 (Fig. 11).

The validation results showed that bias in EF estimates from both observed and interpolated MODIS-T_s was very small, as low as -0.02-0.01, at EF-14 site (Table II), whereas bias was comparatively higher, ranging from 0.03 to 0.1, at EF-21 site (Table II). Likewise, bias in ET estimates was in the range of ±2 Wm^{-2} at EF-14 (Table III), while 13.4-21.3 Wm^{-2} bias was seen at EF-21 (Table III). Afternoon T_s (0.15 RMSE) was slightly better than morning T_s (0.14 RMSE) at modeling EF variation at EF-14, respectively. Less accurate EF estimates were respectively obtained by both morning and afternoon T_s with 0.186 and 0.187 RMSEs at EF-21. This is because $T_s - T_a$ is not a good indicator of both α and EF outside the growing season of the deciduous forest, and the model performed relatively poor at estimating EFs outside the growing season (Figure 10). However, several modifications to the model, which will be discussed in Section 4.1, are proposed to minimize this issue and improve the accuracy over deciduous forests.

As expected, the model performed slightly better at

estimating diurnal EF with observed T_s in comparison to interpolated T_s (Table II) due to the fact that observed T_s was more accurate than interpolated T_s (Table I). RMSEs in EFs estimated by interpolated T_s varied between 0.150 and 0.157 in comparison to RMSEs of 0.131-0.147 in EFs computed from observed T_s at EF-14. Similarly, RMSEs of 0.177-0.178 in EFs increased to 0.205-0.207 when EFs were estimated by interpolated MODIS-T_s at EF-21.

It is worth pointing out that model performance should be examined based on the RMSEs in EF estimates (Table II) as opposed to ET estimates (Table III) because small EF errors during the growing season would result in large ET errors in Wm^{-2} units, while large EF errors outside the growing season when the available energy is relatively low would yield small ET errors in Wm^{-2} units. Finally, the model when run with morning and afternoon T_s respectively yielded 39.3 Wm^{-2} and 34.9 Wm^{-2} RMSEs at EF-14, and 60.74 Wm^{-2} and 61.63 Wm^{-2} RMSEs at EF-21 (Table III).

IV. Discussion

In this section, possible modifications to the model are discussed to improve EF estimates and achieve a better accuracy outside the growing season for forest ecosystems. Next, underlying factors behind the discrepancy seen between modeled and observed EF and ET estimates is described in detail. In the end, how sensitive the trapezoid model is to errors in the input data is analyzed and presented.

A. Potential Improvements to the model

In contrast to the strong relation of $T_s - T_a$ to α and EF during the growing season, T_s is not coupled with ET processes when the forest ecosystem is inactive (Figs. 6 & 7). Thus, more accurate EF results were observed at the winter wheat site (EF-14) in comparison to the deciduous forest site (EF-21) overall in 2011. However, it was shown that α hovers around 0.20 when water is the limiting factor to ET at deciduous forest site. Therefore, such information can be used to improve the accuracy of EF estimates at the deciduous forest site outside the growing season.

We propose that α can be set to 0.2 only for dry days outside the growing season. For wet days which follow a major PRCP event (>3 mm), α can be estimated by the model. However, the proposed modification comes with the cost of incorporating four more variables into the model such as land cover map to identify forest ecosystems, PRCP maps to distinguish dry days from wet days, and SOS and EOS maps (one map per year each). After the proposed changes were applied, RMSEs in morning and afternoon EFs respectively reduced from 0.186 and 0.187 to 0.142 and 0.138 at the deciduous forest. Likewise, accuracy in ET estimates improved by approximately 10 Wm^{-2}, and RMSEs in morning and afternoon ETs reduced to 50.674 Wm^{-2} and 49.886 Wm^{-2} from 60.737 Wm^{-2} and 61.631 Wm^{-2}, respectively (Table IV). Moreover, large errors in small ETs outside the growing season (Fig. 10) are considerably eliminated, thereby agreeing very well with flux tower ET estimates (Fig. 12). This modification is only needed at forest sites outside the growing season when forests are not photosynthetically active. For applications inside the growing season, the basic model can be used without any tweak.

B. Causes of differences between modeled and observed estimates

The causes of discrepancy between observed and modeled EF/ET estimates can be summarized in three sub-topics as follows:

1. Uncertainties in H, LE, R_n and G collectively causes 25-30% discrepancy in energy balance closure [30], [38] due to inherent errors in ECOR measurements such as underestimated or erroneous fluxes under low wind speeds (less 1.5 m/s) and non-steady atmospheric conditions, omission of canopy energy storage in energy balance, and sonic anemometer frequency measurement limitations [29]. Therefore, satellite-based EF and LE estimates likely differ from ground-based estimates due to the issues with regard to flux measurement, energy balance closure and errors in input variables.
2. Footprint mismatch between flux towers (≈100 m) [39] and satellite (1 km), and surface heterogeneity within the ground sample area that satellite views from the space [5], [40], [41]. Thus, satellite EF and ET estimates are a spatially representative of much larger area ($1km^2$) than tower-based estimates.
3. Simplification of mechanisms behind ET process at the expense of accuracy. On the other hand, simplification enables us to reduce the number of forcing and input/in-situ data required to estimate EF and ET. Otherwise small errors in these inputs would be propagated to the final output and lead to larger biases and errors [5].

C. Sensitivity Analysis

The sensitivity of the trapezoid model to the errors in NDVI, T_s, T_a and z was examined. Using the wet and dry edges on June 22, 2011, ±5% and ±10% errors were independently added to observed T_s, T_a, NDVI and z values. Later, EFs and LEs were separately recalculated from these inputs (Table V). Results indicated that +/-1.7675 °C and +/-3.535 °C errors in T_s respectively induced -/+0.069 and -/+0.138 errors in EF estimates which translated to -/+27.623 Wm^{-2} and -/+55.246 Wm^{-2} errors in LE estimates on June 22, 2011 when the available energy was equal to 401.77 Wm^{-2}. Likewise, +/-1.325 °C and +/-2.65 °C errors in T_a caused about +/-0.056-0.057 (+/-22-23 Wm^{-2}) and +/-0.109-0.115 (+/-44-46 Wm^{-2}) errors in EF (LE) estimates. On the other hand, modest errors in EF and LE were observed by the errors in NDVI and z. For NDVI, +/-0.035 and +/-0.070 errors resulted in nearly -/+0.026-0.027 (-/+10-11 Wm^{-2}) and -/+0.050-0.056 (-/+20-22 Wm^{-2}) errors, in EF (LE) estimates. For z, ±10.45 m and ±20.9 m errors yielded insignificant errors in LE and EF (less than 0.001 and 0.1 Wm^{-2}). This sensitivity analysis implies that underestimation in NDVI and T_a would cause overestimation in EF and LE, whereas positive errors in T_a would lead to overestimation. Overall, in the descending order, the trapezoid model is sensitive to errors in T_s, T_a, NDVI and z.

V. Conclusions

In this study, we demonstrated the feasibility of generating spatially-continuous daily EF and ET from minimal (4 inputs for EF and 6 inputs for ET estimation) remotely-sensed and meteorological inputs in a trapezoidal framework both cloud-free and partial-cloudy conditions. Satellite estimates were validated at two Eddy correlation flux towers in Southern Great Plains. Finally, we examined sensitivity of the model to the errors in input variables.

It can be concluded that the gradient of $T_s - T_a$ is negatively correlated with both α and EF on a daily basis. This negative relationship is relatively strong during high evaporative months in comparison to cold months when vegetation is dormant. Moreover, the use of $T_s - T_a$ confirms that α and EF decrease by going from small $T_s - T_a$ to large $T_s - T_a$ as in employed in the trapezoidal model.

The most critical variable in the model is T_s, as EF is most sensitive to errors in T_s followed by T_a. The model is least sensitive to errors in z and NDVI. Overall, negative errors in T_s and NDVI, and positive errors in T_a cause overestimation in EF and subsequently ET.

Biases were small in both modeled EFs and ETs (Figs. 11 & 12) because impact of systematic errors in the input forcing data is minimized as α is estimated based on the relative position to the trapezoidal shape. Likewise, differences of T_s values obtained 1.5 and 5.5 hour after local sunrise are used in the TSEB and TSEB-based ALEXI models to minimize the effect of bias in absolute T_s [8]. However, TSEB model when combined with MODIS-T_s difference of day and night (Ts difference of 1.5 and 5.5 hour after local sunrise are not available from MODIS) overestimated H and underestimated LE because different biases were observed with the day (positive) and night MODIS-T_s (negative) [42].

It can be concluded (based on RMSEs in EFs from observed T_s) that the model performed more accurately with afternoon T_s (Aqua) than morning T_s (Terra) at both winter wheat (Table II) and deciduous forest (Table IV) sites. EF estimates computed from interpolated MODIS-T_s are less accurate compared to EF estimates from observed MODIS-Ts. Because there are two diurnal EF estimates from Terra and Aqua satellites per day, Terra-based EFs can be employed to fill the gaps in Aqua-based EFs. If any gaps remain, these interpolated EFs can be further used to construct a complete annual or growing season of EF and ET estimates.

Another advantage is that the model is not restricted to clear-sky days and directly provides a diurnal EF estimate. In this case, there is no need to make an assumption that EF is constant or self-preserved during daytime to go from instantaneous estimate at the satellite overpass time to daytime estimate. Gentine et al. [43] revisited this assumption and expressed that EF is only constant under high relative humidity and solar radiation conditions.

Croplands are subject to more anthropogenic influences than natural ecosystems. Therefore, gap filling of T_s by interpolation likely induces larger errors over croplands (Table I). Unlike NDVI time series obtained at EF-21 (Fig. 5), planting and harvesting dates of wheat cannot be estimated by the coarse (1 Km) NDVI increase and decrease. After the harvest of winter wheat, the NDVI value was still high due to mixed and aggregated grassland and winter wheat signals (Fig. 5).

The trapezoid model is able to produce accurate EF and ET estimates when evaporative demand is high and temperatures are warm enough to support vegetation growth. However, the accuracy is considerably compromised outside the growing season at deciduous forest due to the fact that $T_s - T_a$ is not a reliable indicator of EF (Fig. 6b). This further implies that T_s is coupled with ET only if transpiration rather than evaporation dominates ET, because a strong link of $T_s - T_a$ with ET was only observed within the months when vegetation is photosynthetically active (Figs. 6 & 7). However, proposed modifications to the model are able to improve the model accuracy at the deciduous forest site outside the growing season at the expense of adding more variables to the model.

Finally, the outputs of this model, regional daily MODIS-EF and -ET maps, can be used in the calibration and validation of hydrological, climate, and land surface models. The model can be run in other regions since the model inputs are largely satellite-based and easily obtainable for other regions as demonstrated in Florida, Everglades [18]. The model can be tuned/adjusted based on land cover and regional characteristics (work in progress). Furthermore, the MODIS-based EF maps can be used in drought monitoring applications [44].

There is another project, namely MOD16, that produces a 1km MODIS-ET datasets on a 8-day, monthly and annual basis [45]. Unlike here, T_s is not incorporated into its ET algorithm, Penman-Monteith approach, which requires calibration by tower-based ET data. MOD16 inputs include MODIS-derived LAI and the Fraction of Absorbed Photosynthetically Active Radiation (FPAR) and a large set of meteorological inputs based on reanalysis dataset produced by the NASA's Global Modeling and Assimilation Office (GMAO). Although MOD16-ET products are not tested and validated at EF-14 and EF-21, both Ramoelo et al. [46] and Tang et al. [47] found poor and inconsistent results in African Savanna ecosystem and irrigated lands in North China when MOD16-ET estimates were compared to flux tower ET estimates on a 8-day interval, respectively. Besides, RMSEs of ET estimates were reported to be as high as observed ET estimate [45].

Acknowledgment

This research was supported by an appointment to the NASA Postdoctoral Program at the Goddard Space Flight Center, administered by Universities Space Research Association through a contract with NASA. Authors thank David Cook of Argonne National Laboratory for providing assistance and information about the validation data and validation sites.

References

[1] B. Mueller *et al.*, "Benchmark products for land evapotranspiration: LandFlux-EVAL multi-data set synthesis," *Hydrol. Earth Syst. Sci.*, vol. 17, no. 10, pp. 3707–3720, Oct. 2013.

[2] J. A. Santanello, C. D. Peters-Lidard, S. V. Kumar, C. Alonge, and W.-K. Tao, "A Modeling and Observational Framework for Diagnosing Local Land–

Atmosphere Coupling on Diurnal Time Scales," *J. Hydrometeorol.*, vol. 10, no. 3, pp. 577–599, Jun. 2009.
[3] C. Jiménez *et al.*, "Global intercomparison of 12 land surface heat flux estimates," *J. Geophys. Res.*, vol. 116, no. D2, p. D02102, Jan. 2011.
[4] B. Mueller *et al.*, "Evaluation of global observations-based evapotranspiration datasets and IPCC AR4 simulations," *Geophys. Res. Lett.*, vol. 38, no. 6, p. L06402, Mar. 2011.
[5] M. F. McCabe, A. Ershadi, C. Jimenez, D. G. Miralles, D. Michel, and E. F. Wood, "The GEWEX LandFlux project: evaluation of model evaporation using tower-based and globally gridded forcing data," *Geosci Model Dev*, vol. 9, no. 1, pp. 283–305, Jan. 2016.
[6] G. Badgley, J. B. Fisher, C. Jiménez, K. P. Tu, and R. Vinukollu, "On Uncertainty in Global Terrestrial Evapotranspiration Estimates from Choice of Input Forcing Datasets," *J. Hydrometeorol.*, vol. 16, no. 4, pp. 1449–1455, Mar. 2015.
[7] Y. Xia, M. T. Hobbins, Q. Mu, and M. B. Ek, "Evaluation of NLDAS-2 evapotranspiration against tower flux site observations," *Hydrol. Process.*, vol. 29, no. 7, pp. 1757–1771, Mar. 2015.
[8] M. C. Anderson, J. M. Norman, J. R. Mecikalski, J. A. Otkin, and W. P. Kustas, "A climatological study of evapotranspiration and moisture stress across the continental United States based on thermal remote sensing: 1. Model formulation," *J. Geophys. Res.*, vol. 112, no. D10, p. D10117, May 2007.
[9] M. C. Anderson and W. Kustas, "Thermal Remote Sensing of Drought and Evapotranspiration," *Eos Trans. Am. Geophys. Union*, vol. 89, no. 26, p. 233, 2008.
[10] T. N. Carlson, "An Overview of the 'Triangle Method' for Estimating Surface Evapotranspiration and Soil Moisture from Satellite Imagery," *Sensors*, vol. 7, no. 8, pp. 1612–1629, Aug. 2007.
[11] M. S. Moran, T. R. Clarke, Y. Inoue, and A. Vidal, "Estimating crop water deficit using the relation between surface-air temperature and spectral vegetation index," *Remote Sens. Environ.*, vol. 49, no. 3, pp. 246–263, Sep. 1994.
[12] J. M. Norman, W. P. Kustas, and K. S. Humes, "A two-source approach for estimating soil and vegetation energy fluxes in observations of directional radiometric surface temperature," *Agric. For. Meteorol.*, vol. 77, no. 3–4, pp. 263–293, Dec. 1995.
[13] W. G. M. Bastiaanssen, M. Menenti, R. A. Feddes, and A. A. M. Holtslag, "A remote sensing surface energy balance algorithm for land (SEBAL). 1. Formulation," *J. Hydrol.*, vol. 212–213, pp. 198–212, Dec. 1998.
[14] R. G. Allen, M. Tasumi, and R. Trezza, "Satellite-Based Energy Balance for Mapping Evapotranspiration with Internalized Calibration (METRIC)—Model," *J. Irrig. Drain. Eng.*, vol. 133, no. 4, pp. 380–394, Aug. 2007.
[15] M. Choi, W. P. Kustas, M. C. Anderson, R. G. Allen, F. Li, and J. H. Kjaersgaard, "An intercomparison of three remote sensing-based surface energy balance algorithms over a corn and soybean production region (Iowa, U.S.) during SMACEX," *Agric. For. Meteorol.*, vol. 149, no. 12, pp. 2082–2097, Dec. 2009.
[16] J. Sheffield, G. Goteti, and E. F. Wood, "Development of a 50-year high-resolution global dataset of meteorological forcings for land surface modeling," *J. Clim.*, vol. 19, pp. 3088–3111, Jul. 2006.
[17] A. L. Yagci, J. A. Santanello, and J. W. Jones, "A Satellite-Based Estimation of Evapotranspiration Using Vegetation Index-Temperature Trapezoid Concept: A Case Study in Southern Florida, U.S.A.," in *American Geophysical Union (AGU) Fall Meeting 2015*, San Francisco, CA, USA, 2015.
[18] A. L. Yagci, J. A. Santanello, J. W. Jones, and J. Barr, "Estimating evaporative fraction from readily obtainable variables in mangrove forests of the Everglades, U.S.A.," *Int. J. Remote Sens.*, vol. 38, no. 14, pp. 3981–4007, Jul. 2017.
[19] T. N. Carlson and D. A. Ripley, "On the relation between NDVI, fractional vegetation cover, and leaf area index," *Remote Sens. Environ.*, vol. 62, no. 3, pp. 241–252, Dec. 1997.
[20] J. A. Santanello and T. N. Carlson, "Mesoscale Simulation of Rapid Soil Drying and Its Implications for Predicting Daytime Temperature," *J. Hydrometeorol.*, vol. 2, no. 1, pp. 71–88, Feb. 2001.
[21] C. H. B. Priestley and R. J. Taylor, "On the Assessment of Surface Heat Flux and Evaporation Using Large-Scale Parameters," *Mon. Weather Rev.*, vol. 100, no. 2, pp. 81–92, Feb. 1972.
[22] R. G. Allen, L. S. Pereira, D. Raes, and M. Smith, *Crop Evapotranspiration: Guidelines for Computing Crop Water Requirements*. Rome, Italy: FAO - Food and Agriculture Organization of the United Nations, 1998.
[23] A. Jarvis, H. I. Reuter, A. Nelson, and E. Guevara, "1-km Hole-filled SRTM for the globe Version 4.1," *Available CGIAR-CSI SRTM 90m Database*, 2008.
[24] T. N. Carlson, E. M. Perry, and T. J. Schmugge, "Remote estimation of soil moisture availability and fractional vegetation cover for agricultural fields," *Agric. For. Meteorol.*, vol. 52, no. 1–2, pp. 45–69, Aug. 1990.
[25] Atmospheric Radiation Measurement Climate Research Facility, "Quality Controlled Eddy Correlation Flux Measurement (30QCECOR). 2003-09-12 to 2015-12-31, 36.607 N 97.488 W: Southern Great Plains (SGP) Lamont, OK (Extended, secondary) (E14)," *Atmospheric Radiat. Meas. ARM Clim. Res. Facil. Data Arch. Oak Ridge Tenn. USA*, 2003.
[26] Atmospheric Radiation Measurement Climate Research Facility, "Quality Controlled Eddy Correlation Flux Measurement (30QCECOR). 2004-02-11 to 2015-12-31, 35.615 N 96.065 W: Southern Great Plains (SGP) Okmulgee, OK (Extended) (E21)," *Atmospheric Radiat. Meas. ARM Clim. Res. Facil. Data Arch. Oak Ridge Tenn. USA*, 2003.
[27] Atmospheric Radiation Measurement Climate Research Facility, "Surface Energy Balance System (SEBS). 2010-10-19 to 2016-06-22, 36.607 N 97.488 W: Southern Great Plains (SGP) Lamont, OK (Extended, secondary) (E14)," *Atmospheric Radiat. Meas. ARM Clim. Res. Facil. Data Arch. Oak Ridge Tenn. USA*, 2010.
[28] Atmospheric Radiation Measurement Climate Research Facility, "Surface Energy Balance System (SEBS). 2010-10-21 to 2016-06-22, 35.615 N 96.065 W: Southern Great Plains (SGP) Okmulgee, OK (Extended) (E21)," *Atmospheric Radiat. Meas. ARM Clim. Res. Facil. Data Arch. Oak Ridge Tenn. USA*, 2010.
[29] D. R. Cook, "Eddy Correlation Flux Measurement System (ECOR) Instrument Handbook," Department of Energy Atmospheric Radiation Measurement (ARM) Program, Oklahoma, U.S.A., DOE/SC-ARM/TR-052, Jan. 2016.
[30] W. P. Kustas, J. H. Prueger, K. S. Humes, and P. J. Starks, "Estimation of Surface Heat Fluxes at Field Scale Using Surface Layer Versus Mixed-Layer Atmospheric Variables with Radiometric Temperature Observations," *J. Appl. Meteorol.*, vol. 38, no. 2, pp. 224–238, Feb. 1999.
[31] G. Hulley and S. Hook, "ASTER Global Emissivity Dataset, 100-meter, HDF5," *NASA EOSDIS Land Process. DAAC USGS Earth Resour. Obs. Sci. EROS Cent. Sioux Falls S. D. USA*, 2014.
[32] Atmospheric Radiation Measurement Climate Research Facility, "Surface Meteorological Instrumentation (MET). 1999-07-27 to 2016-06-25, 35.615 N 96.065 W: Southern Great Plains (SGP) Okmulgee, OK (Extended) (E21)," *Atmospheric Radiat. Meas. ARM Clim. Res. Facil. Data Arch. Oak Ridge Tenn. USA*, 1993.
[33] Atmospheric Radiation Measurement Climate Research Facility, "Surface Meteorological Instrumentation (MET). 1993-07-21 to 2016-06-25, 36.605 N 97.485 W: Southern Great Plains (SGP) Lamont, OK (Extended) (E13)," *Atmospheric Radiat. Meas. ARM Clim. Res. Facil. Data Arch. Oak Ridge Tenn. USA*, 1993.
[34] R. Solano, K. Didan, A. Jacobson, and A. R. Huete, "MODIS Vegetation Index (MOD13) C5 User's Guide Version 2," Vegetation Index and Phenology Lab, The University of Arizona, 2010.
[35] Z. Wan, "Collection-5 MODIS Land Surface Temperature Products Users' Guide," Institute for Computational Earth System Science, University of California, Santa Barbara, CA, USA, Sep. 2006.
[36] P. E. Thornton *et al.*, "Daymet: Daily Surface Weather Data on a 1-km Grid for North America, Version 2," *Oak Ridge Natl. Lab. Distrib. Act. Arch. Cent. Oak Ridge Tenn. USA*, 2014.
[37] P. E. Thornton, S. W. Running, and M. A. White, "Generating surfaces of daily meteorological variables over large regions of complex terrain," *J. Hydrol.*, vol. 190, no. 3–4, pp. 214–251, Mar. 1997.
[38] T. E. Twine *et al.*, "Correcting eddy-covariance flux underestimates over a grassland," *Agric. For. Meteorol.*, vol. 103, no. 3, pp. 279–300, Jun. 2000.
[39] J. M. Norman *et al.*, "Remote sensing of surface energy fluxes at 10-m pixel resolutions," *Water Resour. Res.*, vol. 39, no. 8, p. 1221, Aug. 2003.
[40] S. Wang *et al.*, "Comparing Evapotranspiration from Eddy Covariance Measurements, Water Budgets, Remote Sensing, and Land Surface Models over Canada," *J. Hydrometeorol.*, vol. 16, no. 4, pp. 1540–1560, Mar. 2015.
[41] B. Wu, W. Zhu, N. Yan, X. Feng, Q. Xing, and Q. Zhuang, "An Improved Method for Deriving Daily Evapotranspiration Estimates From Satellite Estimates on Cloud-Free Days," *IEEE J. Sel. Top. Appl. Earth Obs. Remote Sens.*, vol. 9, no. 4, pp. 1323–1330, Apr. 2016.
[42] R. Guzinski, M. C. Anderson, W. P. Kustas, H. Nieto, and I. Sandholt, "Using a thermal-based two source energy balance model with time-differencing to estimate surface energy fluxes with day–night MODIS observations," *Hydrol Earth Syst Sci*, vol. 17, no. 7, pp. 2809–2825, Jul. 2013.
[43] P. Gentine, D. Entekhabi, and J. Polcher, "The Diurnal Behavior of Evaporative Fraction in the Soil–Vegetation–Atmospheric Boundary Layer Continuum," *J. Hydrometeorol.*, vol. 12, no. 6, pp. 1530–1546, Apr. 2011.

[44] M. C. Anderson *et al.*, "An Intercomparison of Drought Indicators Based on Thermal Remote Sensing and NLDAS-2 Simulations with U.S. Drought Monitor Classifications," *J. Hydrometeorol.*, vol. 14, no. 4, pp. 1035–1056, Aug. 2013.
[45] Q. Mu, M. Zhao, and S. W. Running, "Improvements to a MODIS global terrestrial evapotranspiration algorithm," *Remote Sens. Environ.*, vol. 115, no. 8, pp. 1781–1800, Aug. 2011.
[46] A. Ramoelo, N. Majozi, R. Mathieu, N. Jovanovic, A. Nickless, and S. Dzikiti, "Validation of Global Evapotranspiration Product (MOD16) using Flux Tower Data in the African Savanna, South Africa," *Remote Sens.*, vol. 6, no. 8, pp. 7406–7423, Aug. 2014.
[47] R. Tang *et al.*, "Multiscale Validation of the 8-day MOD16 Evapotranspiration Product Using Flux Data Collected in China," *IEEE J. Sel. Top. Appl. Earth Obs. Remote Sens.*, vol. 8, no. 4, pp. 1478–1486, Apr. 2015.

Ali L. Yagci received B.S. and M.S. degrees in Geomatics Engineering from Istanbul Technical University, Istanbul, Turkey in 2006 and 2008, respectively. In 2015, he received the Ph.D. degree in Geography and GeoInformation Science from George Mason University, Virginia, U.S.A.

He is currently a post-doctoral fellow in the Hydrological Science Laboratory at NASA's Goddard Space Flight Center. His research interests include drought monitoring and forecasting, and evapotranspiration modeling using remote sensing data and methods.

Joseph A. Santanello received B.S. and M.S. degrees in Meteorology from Rutgers University, New Jersey, U.S.A. and the Pennsylvania State University, Pennsylvania, U.S.A. in 1996 and 1999, respectively. In 2005, he received the Ph.D. degree in Geography from Boston University, Massachusetts, U.S.A.

He is currently a physical scientist in the Hydrological Science Laboratory at NASA's Goddard Space Flight Center. His research interests include Land-Atmosphere coupling of water and energy Cycles, soil moisture-PBL interactions, satellite remote sensing of surface and PBL properties, land surface, PBL, and mesoscale modeling, land data assimilation and calibration.

Table I. Bias and Root Mean Square Error (RMSE) of the comparison between MODIS-T_s and flux tower-T_s (EF-14 and EF-21). n is observation count and r is correlation coefficient.

Sites	Errors	Observed		Interpolated	
		Terra	Aqua	Terra	Aqua
EF-14	n	153	141	90	108
	r	0.97	0.97	0.90	0.91
	Bias (°C)	1.84	4.77	4.40	7.23
	RMSE (°C)*	2.93	2.49	4.75	4.51
EF-21	n	94	90	37	43
	r	0.96	0.95	0.94	0.95
	Bias (°C)	1.36	3.04	1.46	3.59
	RMSE (°C)*	2.49	2.60	3.07	3.24

* RMSE after bias is reduced to zero "0".

Table II. Bias and Root Mean Square Error (RMSE) of the comparison between modeled EFs and observed EFs at the two validation sites, EF-14 and EF-21. n is observation count.

Sites	Errors	Observed		Interpolated		All	
		Terra	Aqua	Terra	Aqua	Terra	Aqua
EF-14	n	153	141	91	108	244	249
	Bias	0.002	-0.021	0.012	-0.004	0.006	-0.013
	RMSE	0.147	0.131	0.154	0.157	0.150	0.142
EF-21	n	94	90	38	45	132	135
	Bias	0.088	0.099	0.026	0.069	0.070	0.089
	RMSE	0.177	0.178	0.207	0.205	0.186	0.187

Table III. Bias and Root Mean Square Error (RMSE) of the comparison between modeled ETs and observed ETs at the two validation sites, EF-14 and EF-21. n is observation count.

Sites	Errors	Observed		Interpolated		All	
		Terra	Aqua	Terra	Aqua	Terra	Aqua
EF-14	n	153	141	91	108	244	249
	Bias (Wm^{-2})	1.589	-4.286	3.325	0.585	2.237	-2.174
	RMSE (Wm^{-2})	40.668	34.077	36.895	35.950	39.304	34.902
EF-21	n	94	90	38	45	132	135
	Bias (Wm^{-2})	18.655	24.708	0.246	14.341	13.355	21.252
	RMSE (Wm^{-2})	60.523	62.780	61.262	59.265	60.737	61.631

Table IV. Bias and Root Mean Square Error (RMSE) in modeled ET at EF-21 deciduous forest site after the proposed improvement to the model only for outside the growing season.

EF/ET	Errors	Before		After	
		Terra	Aqua	Terra	Aqua
EF	n	132	135	132	135
	Bias	0.070	0.089	0.006	0.017
	RMSE	0.186	0.187	0.142	0.138
ET	n	132	135	132	135
	Bias (Wm^{-2})	13.355	21.252	-4.648	0.532
	RMSE (Wm^{-2})	60.737	61.631	50.674	49.886

Table V. Observed errors in Evaporative Fraction (EF) and Latent Heat (LE) on June 22, 2011 after ±5% and 10% errors added to the model variables, NDVI, T_s, T_a and z.

Variables	Errors added ±5%–10%	Observed Errors	
		EF	LE (Wm^{-2})
NDVI	0.0350	-0.027	10.951
	0.0700	-0.056	-22.602
	-0.0350	0.026	10.314
	-0.0700	0.050	20.044
T_s (°C)	1.7675	-0.069	-27.623
	3.5350	-0.138	-55.246
	-1.7675	0.069	27.623
	-3.5350	0.138	55.246
T_a (°C)	1.3250	0.057	22.910
	2.6500	0.115	46.375
	-1.3250	-0.056	-22.312
	-2.6500	-0.109	-43.978
z (m)	10.4500	0.000	0.034
	20.9000	0.000	0.067
	-10.4500	0.000	-0.034
	-20.9000	0.000	-0.067

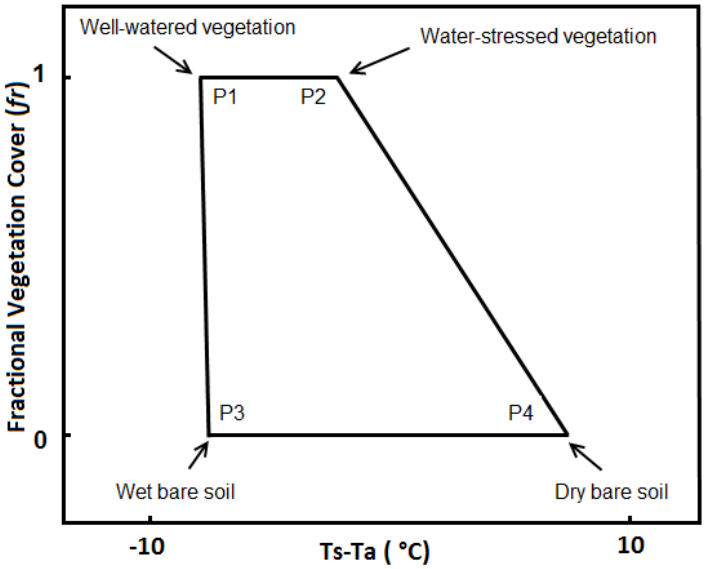

Fig. 1. Theoretical trapezoidal shape that would result from the relation between fractional vegetation cover (Fr) and surface-air temperature difference ($T_s - T_a$).

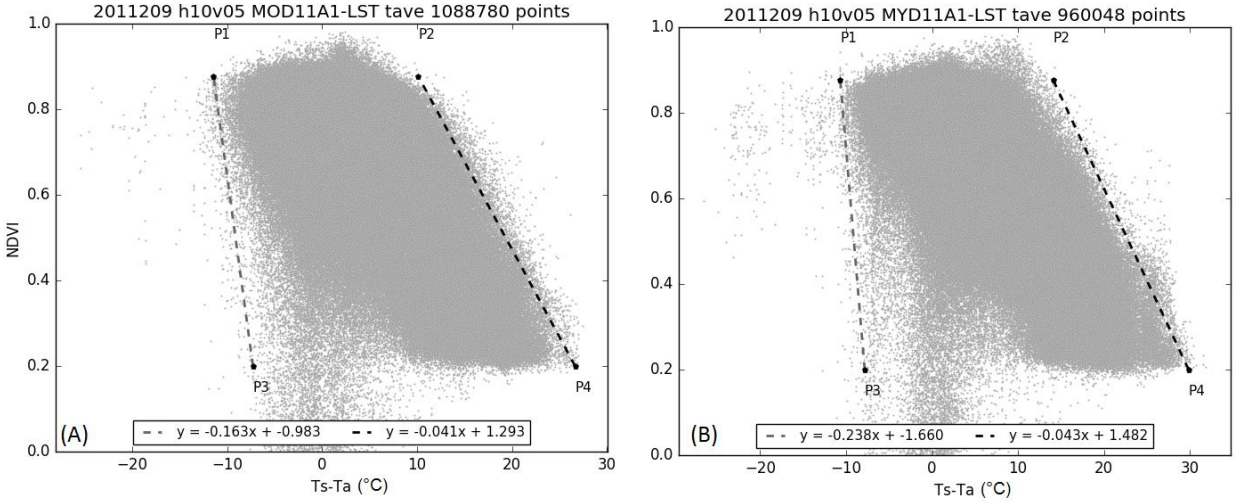

Fig. 2. Scatterplots of ($T_s - T_a$)–NDVI space constructed using T_s from the MODIS instrument onboard Terra (A) and Aqua satellite (B) on July 28, 2011. T_a is the daily average air temperature.

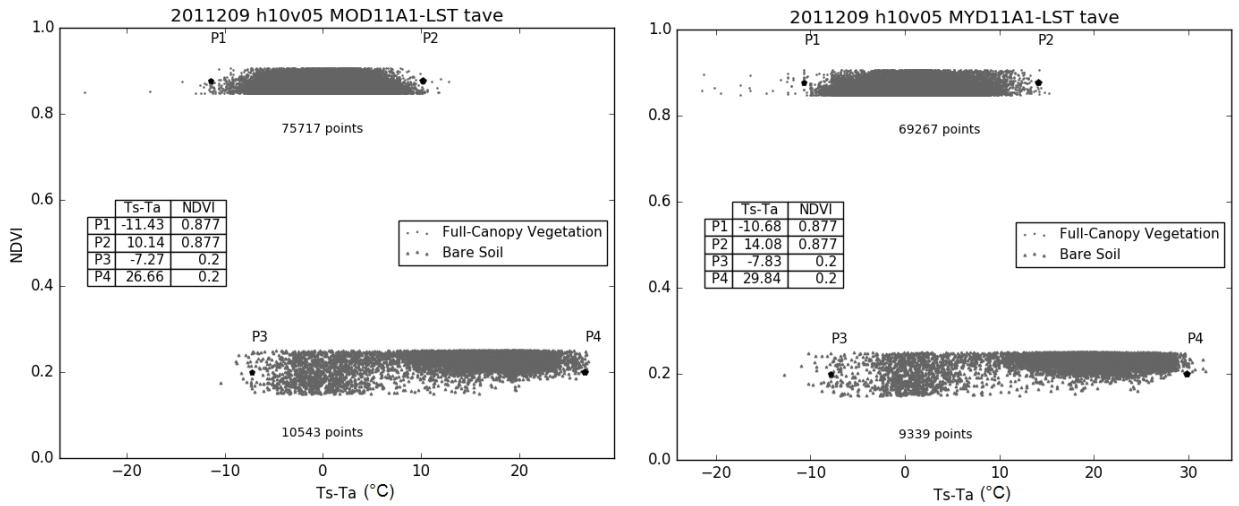

Fig. 3. Distribution of closed-canopy and bare soil points in the two dimensional NDVI–($T_s - T_a$) space on July 28, 2011.

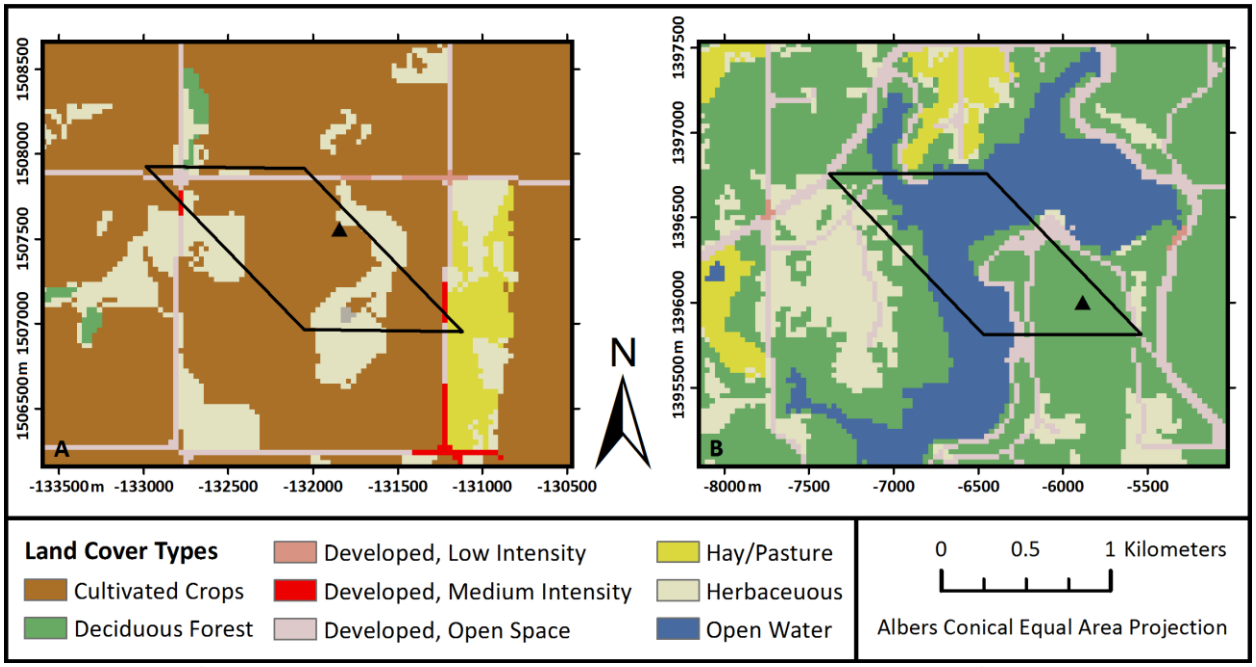

Fig. 4. The location of validation sites, EF-14 (A) and EF-21 (B) with respect to the MODIS pixel ground footprint. Validation sites are shown with the black triangles and the ground footprint of MODIS instrument are shown relative to validation sites with black irregular boxes.

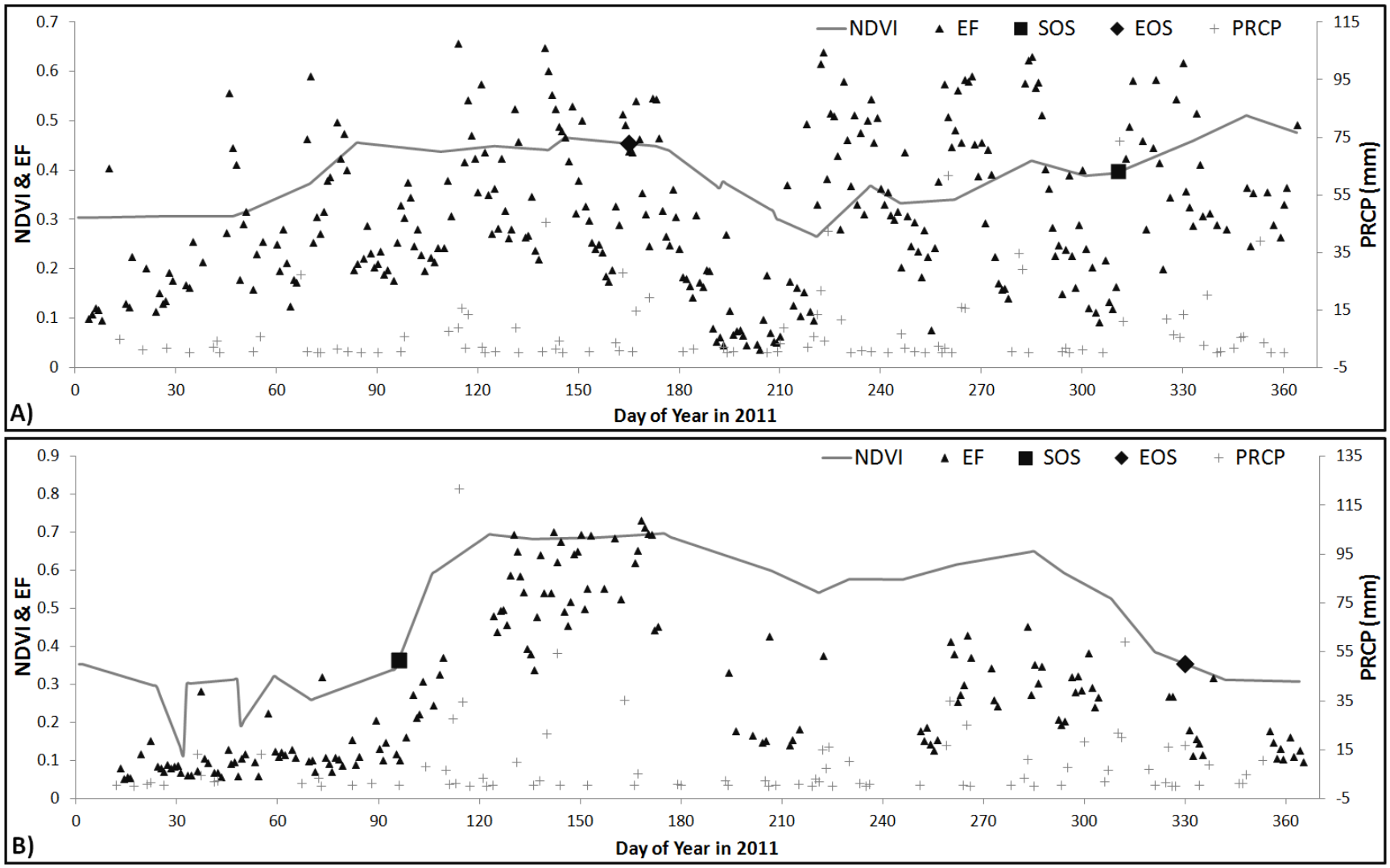

Fig. 5. Variation of NDVI, diurnal Evaporative Fraction (EF), daily Precipitation (PRCP) in 2001 at the ground validation sites, EF-14 (A) and EF-21 (B). Start of Season (SOS) and End of Season (EOS) are also shown on the NDVI time series.

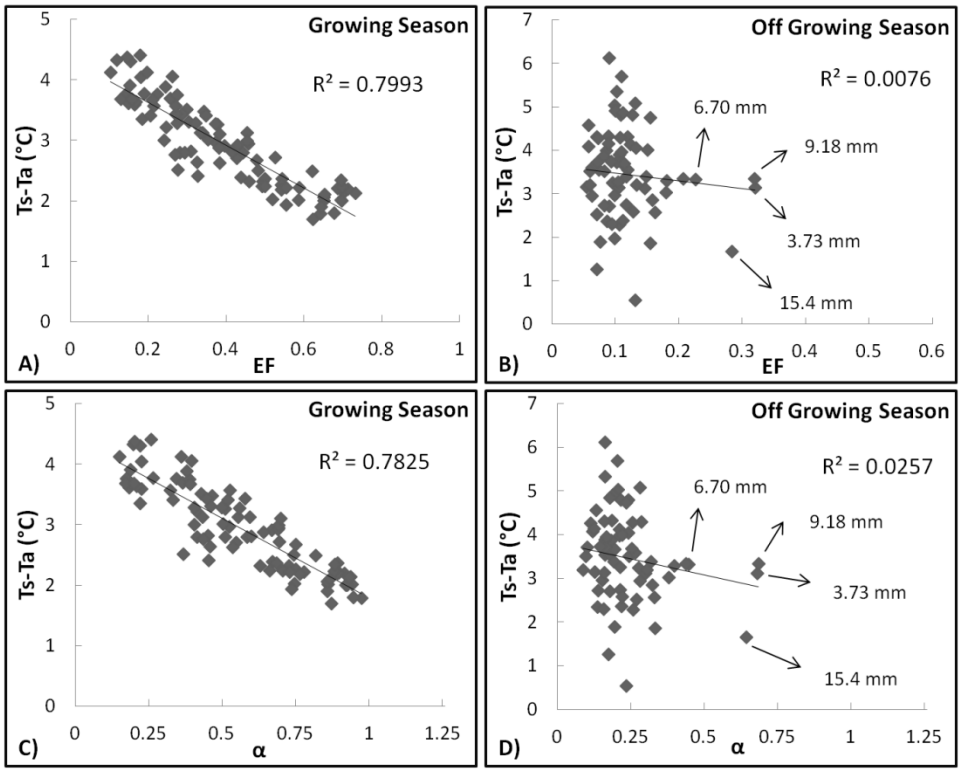

Fig. 6. Variation in Priestley-Taylor coefficient (α) and evaporative fraction (EF) inside and outside the 2011 deciduous forest growing season at EF-21 validation site. Precipitation amounts are shown with arrows only for wet days outside the growing season.

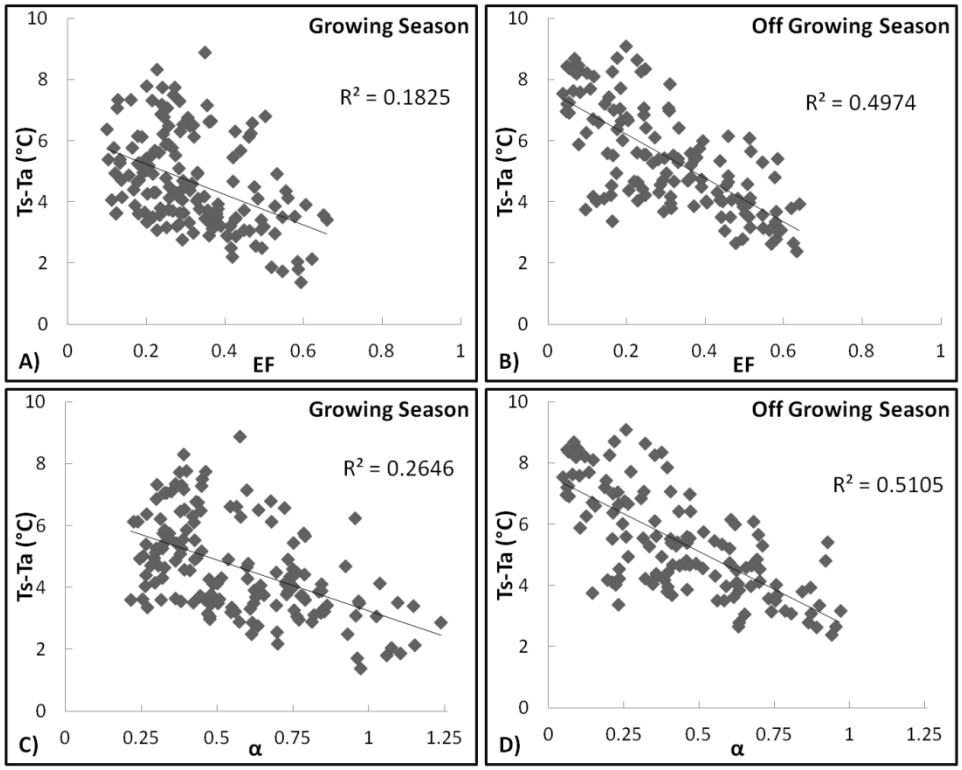

Fig. 7. Variation in Priestley-Taylor coefficient (α) and evaporative fraction (EF) inside and outside the 2011 winter wheat growing season at EF-14 validation site.

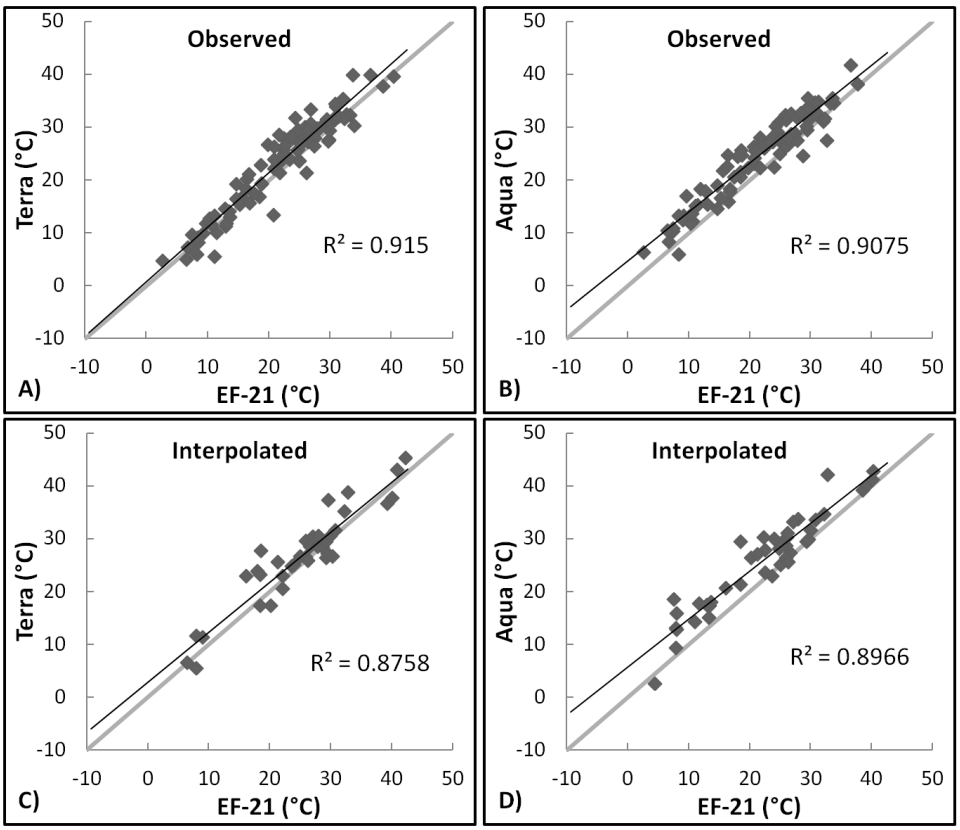

Fig. 8. Comparison of diurnal-mean Land Surface temperature (Ts) observed at EF-21 with observed T_s acquired by MODIS-Terra (A), MODIS-Aqua (B), and gap-filled T_s by interpolation of T_s products from MODIS-Terra (C) and MODIS-Aqua (D).

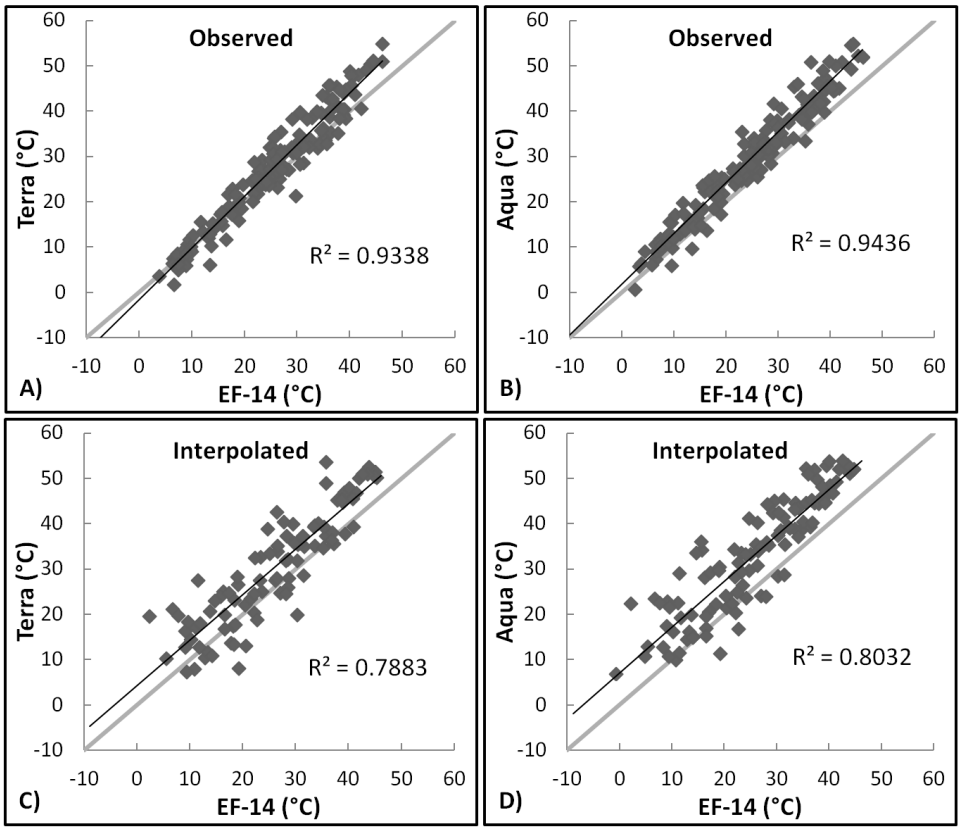

Fig. 9. Comparison of diurnal-mean Land Surface temperature (T_s) observed at EF-14 with observed T_s acquired by MODIS-Terra (A), MODIS-Aqua (B), and gap-filled T_s by interpolation of T_s products from MODIS-Terra (C) and MODIS-Aqua (D).

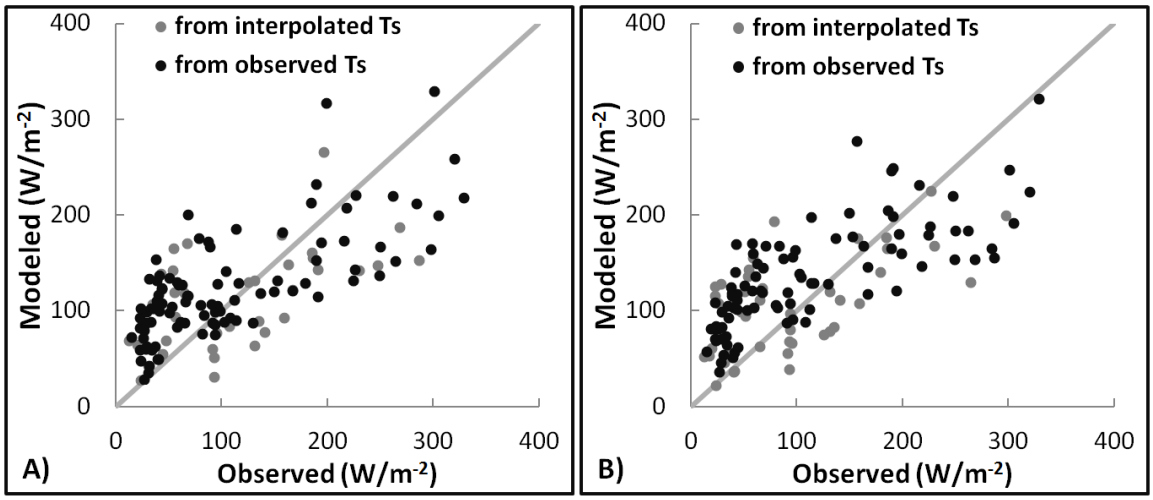

Fig. 10. Comparison between modeled and observed ETs at the deciduous forest site (EF 21). The modeled ETs were calculated from MODIS-T_s products acquired by Terra (A) and Aqua (B) satellites.

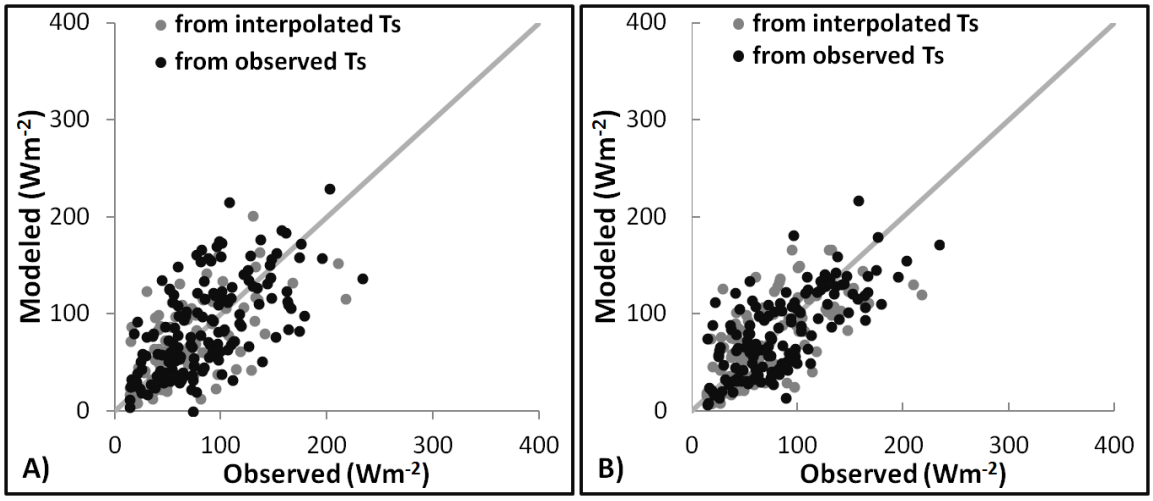

Fig. 11. Comparison between modeled and observed ETs at the winter wheat site (EF 14). The modeled ETs were calculated from MODIS-T_s products acquired by Terra (A) and Aqua (B) satellites.

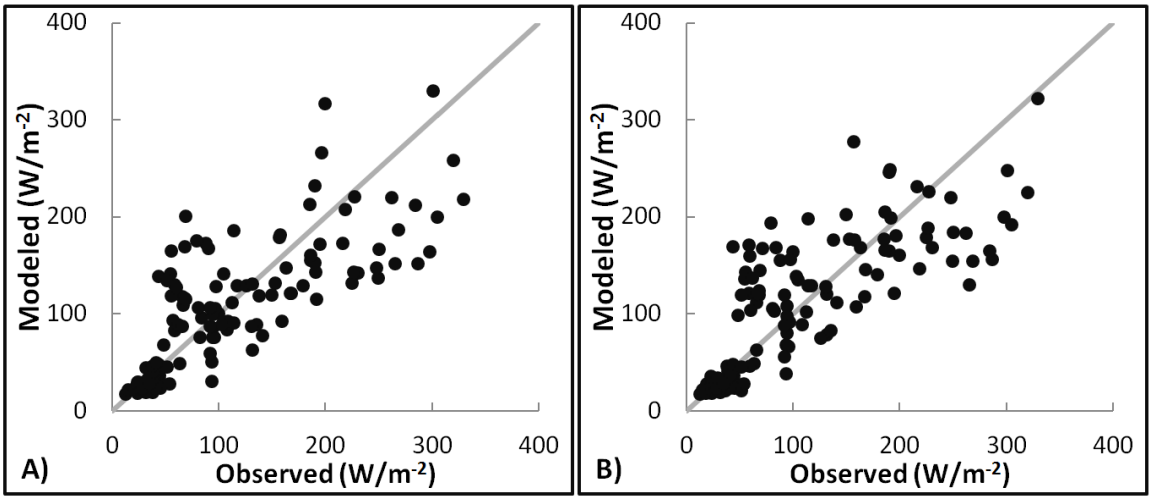

Fig. 12. Comparison between modeled and observed ETs at the deciduous forest site (EF 21) after the modification to the model for off-growing season. The modeled ETs were calculated from MODIS-T_s products acquired by Terra (A) and Aqua (B) satellites.